www.advintellsyst.com

Field-Free Region Scanning-Based Magnetic Microcarrier Targeting in Multibifurcation Vessels

Kim Tien Nguyen, Hyeonwoo Kee, Gwangjun Go, Seok-Jae Kim, Eunpyo Choi, Jong-Oh Park,* Sukho Park,* and Jayoung Kim*

Navigation of microcarriers in complex environments as a vascular network remains an open challenge due to limited solutions for effective targeting strategy. Simultaneous real-time visualization and manipulation of microcarriers at any depth in the human body is far to be achieved even though one of each task has been successfully proven. Herein, a novel targeting strategy is proposed that employs field-free region (FFR) scanning to guide microcarriers through multiple bifurcations within a predefined vessel network. The main challenge of this method lies on how, where, and when to activate FFR to steer a particle to a desired direction, regardless of its spatial feedback. To achieve it, first, a mathematical model of particle motion in a vessel network is developed to predict particle behaviors and positions. Subsequently, an optimization algorithm is formulated to place FFR well-coordinated around each bifurcation at a designated moment. The established solution for targeting a magnetic microcarrier is preemptively evaluated through finite element simulations and then successfully implemented in in vitro multibranched vessels.

1. Introduction

With developing an effective chemotherapeutic drug to kill cancer cells, drug delivery technology for cancer treatment has attracted tremendous effort over the past few decades.^[1-4] There are two main aspects to be addressed for effective drug delivery, including maximizing the access rate to a tumor at a specific site and minimizing the harmfulness to healthy cells while killing cancer cells.^[5] Drug delivery route to be

administered to our body can be selected according to the type and location of cancer and the type of drug, such as oral, injection, and transdermal delivery. [6] The success of drug delivery can be shown by internalizing chemotherapeutic agents in cancer cells and evoking a biological response instead of being removed by the clearance system.^[7] There are two distinct pathways to internalize the agents in the cancer cell. The first method is defined as passive targeting or conventional chemotherapy in which nanocarriers (sizes <100 nm) passively follow the vascular flow after administration into the body. It may incur that the nanocarriers leak into surrounding blood vessels near the cancer site. Thus, this method arises a severe adverse effect on healthy tissues since these chemotherapeutic agents cannot differentiate between normal cells and tumor cells. The second one

is called receptor-mediated active targeting, which conjugates a target moiety with them to preferentially accumulate the drug at the tumor site. Active targeting is usually associated with a type of tumor, and therefore with a specific targeting moiety. These moieties can be chemically conjugated or physically attached to the surface of nanocarriers. [5] However, it is still an open challenge to further increase the therapeutic yield of the active targeting method by improving the accessing rate to the site-specific tumor.

K. T. Nguyen, S.-J. Kim, J.-O. Park, J. Kim Korea Institute of Medical Microrobotics Gwangju 61011, Korea E-mail: jop@kimiro.re.kr; jaya@cbnu.ac.kr

H. Ree, S. Park
Department of Robotics and Mechatronics Engineering
Daegu Gyeongbuk Institute of Science & Technology (DGIST)
Daegu 42988, Korea

E-mail: shpark12@dgist.ac.kr

The ORCID identification number(s) for the author(s) of this article can be found under https://doi.org/10.1002/aisy.202300700.

© 2024 The Authors. Advanced Intelligent Systems published by Wiley-VCH GmbH. This is an open access article under the terms of the Creative Commons Attribution License, which permits use, distribution and reproduction in any medium, provided the original work is properly cited.

DOI: 10.1002/aisy.202300700

O. GO
Department of Mechanical Engineering
Chosun University
Gwangju 61452, Korea

E. Choi School of Mechanical Engineering Chonnam National University Gwangju 61186, Korea

J. Kim Department of Biosystems Engineering Chungbuk National University Cheongju 28644, Korea

www.advancedsciencenews.com

www.advintellsyst.com

Magnetic field manipulation for untethered micro-/nanoobjects has been applied as one of the possible solutions to cope with aforementioned challenges by directly delivering a magnetic microcarrier (MC) from the injection point to the desired location. [8] One of the most straightforward attempts implemented is a directional control of magnetic force, which shows nanocarrier's selective motion at a bifurcation of a blood vessel. [9,10] In this approach, to create the directional magnetic force, a single permanent magnet can be placed next to the desired direction of the bifurcation. [11–15] A multicoil platform can also be used to generate a directional magnetic force at the bifurcation located inside of its workspace. [16-25] This is not quite an efficient way to directly deliver the particle to the target area in aspect of realistic scenarios since the particle has to selectively pass through multiple bifurcations before approaching the targeted region. Modern catheterization may help to reduce the complexity of the task by minimizing the distance between the injection point and the targeted region. However, it is also challenging in the catheter's size limitation (where the catheter cannot access a blood vessel less than twice of its size) and the complexity of catheter guidance into a deep and complex vascular matrix. [26,27] Additionally, despite the catheter use, the carriers need to be controlled to pass at least two more branches before approaching the target, [28] and some of the primary parameters, including the vessel's geometric information, blood flow velocities, and particle specifications, need to be acquired in advance to guide the carriers through multiple branches at high access rate.

There are several efforts performed on multibifurcation targeting by placing multiple soft ferromagnetic balls inside the magnetic resonance imaging (MRI) system,^[8,29] where the position of each magnetic ball is optimized based on the aforementioned primary conditions, desired magnetic force amplitude, and orientation at each bifurcation. This method can successfully deliver MC to a targeted branch in a 3D plastic channel regardless of their current positions. This, however, states a problem in practical trials since the distance between each bifurcation in the

vessel is relatively close (e.g., human hepatic artery), which may reach interference constraints between the cores.^[8] It also requires precise and stable fixation parts of those magnetic balls to match designed positions and avoid strong interaction force between them. Another effort used an interesting alternative magnetic field generated by two electromagnetic coils to selectively pull MC through multiple bifurcation channels using magnetic gradient field. The magnetic force acted on MC to keep them in a safe zone (i.e., an area in front of the bifurcation and on the side where MC was designated to move next). This method was simulated using the finite element (FE) method with different flow rates.^[30] This method required real-time MC position feedback to successfully deliver MC to a targeted area in practical, which currently is a big challenge to be achieved. Even though the most promising imaging technique developed recently for tracking MC inside human body, called magnetic particle imaging (MPI), has relative high sensitivity, high spatial resolution, and high temporal resolution (46 frame/s). [31-34] However, it still cannot be performed simultaneously 3D localization and manipulation of MC. Since the principle of MPI is based on the magnetic response of MC induced by excitation field in a controllable field-free region (FFR) generated by driving coils, [35] while MC movement is controlled by magnetic field or gradient field generated by electromagnetic coils. Therefore, most of the efforts with MPI scanners employed a way to sequentially switch between localization and actuation modes with a limited number of controllable degee of freedom (DOF), 1D.[36] Furthermore, some interesting studies were implemented to simultaneously demonstrate actuation and imaging by modifying FFR scanning trajectory and using it as motion control of MC.[37,38] Nevertheless, none of the currently available targeting schemes satisfy all the requirements for clinical usage.

To tackle the aforementioned challenges, this article proposes a novel targeting scheme utilizing FFR scanning methodology (as depicted in **Figure 1**), and thus the contributions of this study can be succinctly outlined as follows: 1) FFR-based MC targeting

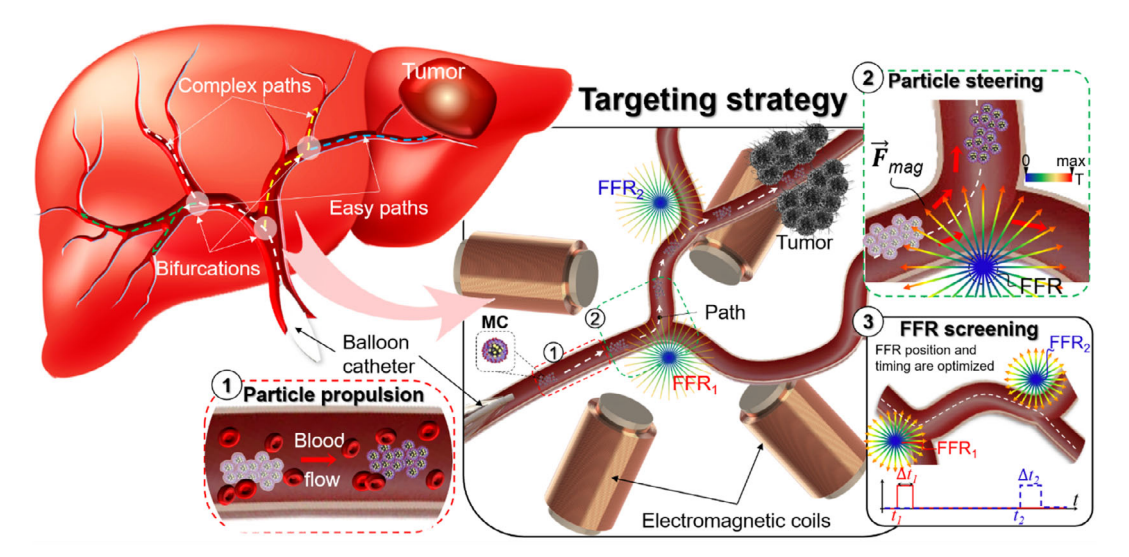


Figure 1. Schematic diagram of the targeting strategy for magnetic nanocarriers by FFR scanning in the complex human liver hepatic arteries with multiple bifurcations: 1) The blood flow acts to push the particle along the blood vessel; 2) at each bifurcation, the particle is steered by sufficient magnetic force induced from generated FFR; and 3) FFRs are scanned along the blood vessel with optimal position and shooting time.

www.advancedsciencenews.com www.advintellsyst.com

strategy: it provides the inaugural methodology of FFR application as a navigation mechanism to actively and effectively guide MCs in intricate vascular networks; 2) Targetable FFR generation methodology: a model-based FFR generation design, for field map, location, and timing prediction, is created to achieve high targeting performance against multiple bifurcations regardless of the particle position feedback from medical imaging devices, such as X-Ray or ultrasound; and 3) Targeting performance validation: the efficacy of the proposed method is substantiated via the dual lenses of FE simulation validation and in-vitro experimental analysis, lending empirical evidence to its effectiveness.

Finally, to evaluate and verify the proposed method, this work mainly utilized an ennead electromagnetic actuation system (EnEMAs) developed in our previous work.^[39,40]

2. Results

2.1. Targeting Strategy for Particle Control in Multibifurcation Vascular Network

The proposed targeting scheme uses the FFR scanning along desired waypoints to steer MC at each bifurcation point to reach a targeted vessel branch. Where the FFR scanning waypoints and scanning time will be optimized using the model-based method. In this section, a precise FFR generation approach, FFR scanning strategy, and the optimized FFR scanning parameters will be presented.

2.1.1. Dynamic Model of the Particle in Vessel

In this work, when the external magnetic field is applied, the dynamic equation of a magnetic particle in the blood vessel (as shown in **Figure 2**) can be expressed as follows

$$m\ddot{\mathbf{x}} = \mathbf{F}_{\text{mag}} + \mathbf{F}_{\text{drag}} \tag{1}$$

where, m, x, F_{mag} and F_{drag} are the mass of the magnetic particle, the position of the magnetic particle, the magnetic force due to the external magnetic field, B and the fluidic drag force exerted on the magnetic particle by the surrounding flow, respectively. The external forces acting on the magnetic particle can be

expressed in detail as follows. First, the magnetic force, $F_{\rm mag}$ can be defined as

$$\mathbf{F}_{\text{mag}} = V(\mathbf{M}(\mathbf{B}) \cdot \nabla)\mathbf{B} = V\left(\mathbf{M}(\mathbf{B}) \frac{\mathbf{B}}{\|\mathbf{B}\|} \cdot \nabla\right)\mathbf{B}$$
(2)

where *V* and **M** are the magnetic particle volume and magnetic moment vector, respectively. Especially, the magnetization of the magnetic particle is depending on the external magnetic field. Therefore, Equation (2) can be rewritten as

$$\mathbf{F}_{\text{mag}} = \mathbf{V} \left(M_{\text{sat}} L(\alpha \| \mathbf{B} \|) \frac{\mathbf{B}}{\| \mathbf{B} \|} \cdot \nabla \right) \mathbf{B}$$
 (3)

where $M_{\rm sat}$ and α are the saturation magnetization and Langevin slope parameter of the magnetic particle, respectively. In this article, the nonlinear magnetization characteristic of the magnetic particle was approximated by utilizing the Langevin function. $L(\gamma) = \coth(\gamma) - \gamma^{-1}$ Here, the value of α that determines the magnetization of the magnetic particle by the external magnetic field $\bf B$ can be extracted from the hysteresis loop of the magnetic particle by fitting the Langevin function on the data. Second, the fluidic drag force can be roughly defined as

$$\mathbf{F}_{\text{drag}} = 3\pi \mu_{\text{fluid}} d_{\text{p}} (\nu_{\text{fluid}} - \dot{\mathbf{x}}) \tag{4}$$

where, $\mu_{\rm fluid}$, $d_{\rm p}$ and $\nu_{\rm fluid}$ denote the dynamic viscosity of the fluid surrounding the magnetic particle, the diameter of the spherical magnetic particle, and the flow velocity around the magnetic particle, respectively. In this article, since the Reynolds number experienced by a magnetic particle in the blood vessel flow can be assumed to be less than 1, it is regarded as resisting the Stokes drag force, which is the fluid drag force. The blood flow in the vessel is a non-Newtonian fluid, meaning that shear stress is not proportional to shear rate. That is, the viscosity is not constant throughout the entire bloodstream. However, in the experimental validation, deionized (DI) water was used for visibility of magnetic particle motion, so a Newtonian fluid with a constant viscosity of 0.001 Pa·s was adopted in the numerical fluid dynamics simulation.

Let us consider the dynamic equation of the particle in blood vessel where the magnetic force will be considered as a control variable for later section. From Equation (1)–(4), it is given as

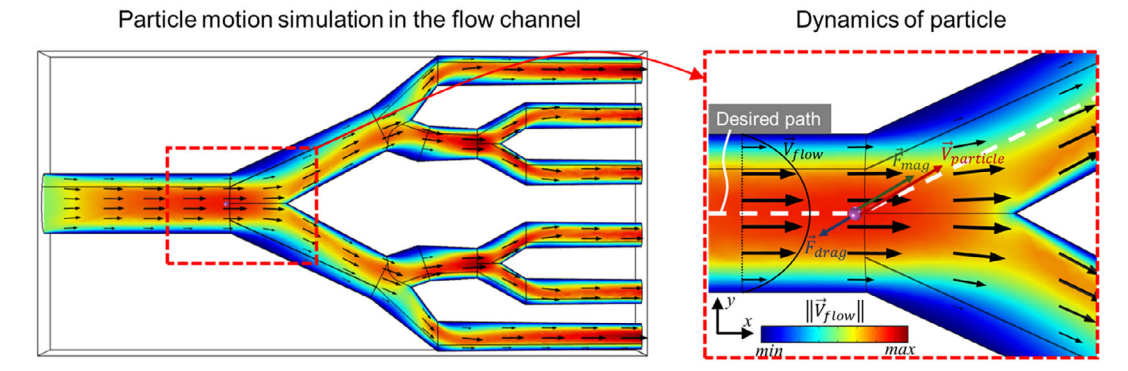


Figure 2. Schematic diagram of hydrodynamics of a magnetic particle in a blood vessel under laminar flow. The magnetic force induced from generated FFR steers the magnetic particle to a desired path at a specific bifurcation. The size of the particle (colored purple) is illustrated with the same size shown in the actual experimental results.

www.advancedsciencenews.com www.advintellsyst.com

$$m\ddot{\mathbf{x}} + 3\pi\mu_{\text{fluid}}d_{\text{p}}\dot{\mathbf{x}} = F_{\text{mag}} + 3\pi\mu_{\text{fluid}}d_{\text{p}}\nu_{\text{fluid}}$$
(5)

Applying Laplace transformation to Equation (5), it is represented as

$$m(s^{2}X - s\mathbf{x}(0) - \dot{\mathbf{x}}(0)) + 3\pi\mu_{\text{fluid}}d_{\text{p}}(sX - \mathbf{x}(0))$$

$$= \frac{1}{s}(\mathbf{F}_{\text{mag}} + 3\pi\mu_{\text{fluid}}d_{\text{p}}\nu_{\text{fluid}})$$
(6)

Given that at each sampling time t_i , $\mathbf{x}(0) = 0$, $\dot{\mathbf{x}}(0) = \nu_0$ Equation (6) can be rewritten as

$$(ms^2 + 3\pi\mu_{\text{fluid}}d_ps)X = \frac{1}{s}(\mathbf{F}_{\text{mag}} + 3\pi\mu_{\text{fluid}}d_p\nu_{\text{fluid}}) + m\nu_0$$
 (7)

$$\Leftrightarrow X = \frac{\mathbf{F}_{\text{mag}} + 3\pi\mu_{\text{fluid}}d_{\text{p}}\nu_{\text{fluid}} + m\nu_{0}s}{ms^{2}\left(s + \frac{3\pi\mu_{\text{fluid}}d_{\text{p}}}{m}\right)}$$
(8)

Let us set, $\frac{\mathbf{F}_{\text{mag}}+3\pi\mu_{\text{fluid}}d_{\text{p}}\nu_{\text{fuid}}}{m}=L\frac{3\pi\mu_{\text{fluid}}d_{\text{p}}}{m}=K$ and substitute them into Equation (8) as

$$X = \frac{v_0 s + L}{s^2 (s + K)} = \left[\frac{A}{s^2} + \frac{B}{s} + \frac{C}{s + K} \right]$$
 (9)

Equalizing the left- and the right-hand side of the numerator of Equation (9) as

$$\begin{cases} (B+C) = 0 \\ A+BK = \nu_0 \\ AK = L \end{cases} \Rightarrow \begin{cases} A = \frac{L}{K} \\ B = \frac{(\nu_0 K - L)}{K^2} \\ C = \frac{(L - \nu_0 K)}{K^2} \end{cases}$$
 (10)

The transformation of the particle traveling in the blood vessel under resultant force can be expressed in Laplace form by substituting Equation (10) into (9) as

$$X = \frac{L}{K} \frac{1}{s^2} + \frac{\nu_0 K - L}{K^2} \left\{ \frac{1}{s} - \frac{1}{s + K} \right\}$$
 (11)

Then, the particle position and traveling velocity at t_i can be obtained as

$$\mathbf{x}(t) = \frac{L}{K}t + \frac{v_0K - L}{K^2}\{1 - e^{-Kt}\}$$
 (12)

$$\mathbf{x}(t) = L/K + (\nu_0 K - L)/Ke^{-Kt}$$
(13)

2.1.2. FFR Scanning Strategy

In general, to guide the magnetic particles through the multiple consecutive bifurcations, a sufficient magnetic force is required at each bifurcation to steer the particle toward a desired path. In this article, a targeting scheme creates a set of magnetic forces to steer the MCs from before entering to passing the bifurcation using FFR, defined as optimal FFR positions inside the boundary of the system workspace. The following addresses the optimal FFR positioning and timing problem for targeting the MCs.

Let us first consider the blood vessel channel used throughout this work (as shown in **Figure 3**). This is a simplified version

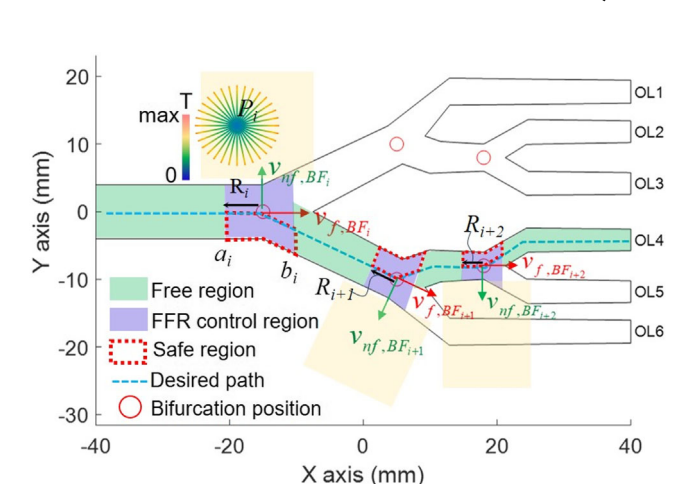


Figure 3. Schematic diagram of the conceptual description of the targeting strategy in a given multibifurcation blood vessel channel using the FFR scanning targeted to OL4. The particle sequentially travels through consecutive free regions (light-green) and FFR control free regions (light-purple). Once the particle enters the i^{th} FCR, it is controlled by magnetic force created by the optimal FFR located at P_i in the FFR $_i$ available region (light-yellow). Here, $\nu_{f,BFi}$, $\nu_{nf,BFi}$, and R_i indicate flow velocity vector, its normal vector, and the vessel radius defined at i^{th} bifurcation, respectively.

of the most common human hepatic artery including one inlet and six outlets where all of the parameters of this channel are predefined.[41] Along a desired path, the quantity of FFR required to be created per each cycle is determined according to the number of bifurcation that MCs have to pass, n_{BE} , which varies from two to three bifurcations. Hereinafter, the affective region where MCs need to be controlled by the magnetic force at each bifurcation is also called as FFR control region (FCR), i.e., starting and ending of this region limited by a distance R_i away from the ith bifurcation, $[a_i, b_i] \in \mathbb{R}^3$ marked in lightpurple region, as shown in Figure 3. The distance R_i is defined as the radius of the vessel at i^{th} bifurcation. This distance was selected to provide sufficient space and time for the MCs to access the safe region under sufficient force, even in the worst-case scenario that MCs stay close to the vessel wall opposite to next desired direction. The safe region (marked as red dashed region, as shown in Figure 3) is located around the bifurcation in the same direction with the next desired direction and bounded by the vessel central line and vessel wall, in which MCs can be correctly steered to the desired direction regardless magnetic force control. The remaining domains of the vessel channel are called free region (green areas in Figure 3). In the free region, the MCs are traveled freely by fluidic flow without magnetic force applied. Considering the equivalence condition of MCs motion in this case (i.e., just drag force remains), the particle velocity, $\dot{\mathbf{x}}(t)$ will equal to flow speed, $v_{\rm fluid}(t)$ From here, the time gap of the first free region can be determined as $[0, t_{FreeEnd,1}]$. $t_{FreeEnd,1}$ is the starting time for the first FCR, t_1 .

The next and main challenge is to determine the ith optimal FFR position, P_i . The FFR used in this targeting task is assumed to be isotropic. At this stage, it serves as an advantage of positioning the FFR with similar magnitude of the magnetic force at different points surrounding P_i with the same distance.



www.advintellsyst.com

www.advancedsciencenews.com

Here, the magnetic force is defined as a function, \mathcal{F} of distance from P, and the magnetic force distribution is used as database in the algorithm later, which is obtained from FE model of the EnEMAs to create FFR at similar gradient input of 1.7 T m⁻¹. A sequential searching method is applied in this work to find out the optimal FFR position at each bifurcation defined as n_{BF} based on a given path (e.g., with the target OL4, $n_{\rm BF} = 3$ as shown in Figure 3). When a magnetic carrier enters the ith FCR, a FFR is created within its available region (light-yellow square region) to steer the MC to a desired direction. The FFR_i available region position, A_{FFR} is defined by its alignment vector, $v_{nf,BF}$ and flow velocity vector, $v_{f,BF}$ at i^{th} bifurcation. The magnitude and orientation of $v_{f,BF}$ are obtained from the FE model of fluidic flow traveling inside the blood vessel channel with various inlet speed, V_{f,data}. Meanwhile, the $v_{nf,BF}$ is a unit vector normal to $v_{f,BF}$ and its direction is opposite to the next desired direction (as shown in Figure 3). The width, w_i and the height, h_i of the FFR_i available region are defined as 4 R_i and $[R_i, max]$, respectively. The i^{th} FFR position varies within this (w_i, h_i) region and stays inside the channel boundary, $-40 \,\mathrm{mm} > x > 40 \,\mathrm{mm}$, $-20 \,\mathrm{mm}$ > y > 20 mm. Thus, to decide ith optimal FFR position, P_i in the FFR_i available region, the MC guiding performance is computationally analyzed based on its aforementioned dynamic model from its initial position to the end of FCR_i. Here, we assumed that the MC initial position always stays in the worst-case scenario. The particle-wall interactions were ignored, while assumed that the particle stays at the channel wall, \mathbf{x}_{col} at the moment when collision occurs. The position error, ξ is calculated as difference between instant particle position and desired way point, x_d. To evaluate optimality of the FFR positioned, three criteria were designed and they must be satisfied to select the optimal FFR position. First, the MC at the end of FCR_i should pass the central line to enter the safe region. It is a condition to prevent the MC from taking unexpected action inducing off target due to insufficient magnetic force applied. Second, the MC should have a reasonable moving direction and velocity to make sure it travels smoothly in FCR_i. At some particular FFR positions, the MC may end up with reverse motion against a desired direction due to strong magnetic force applied in an unintended direction, even if it passes the first criterion. Last but not least, the optimal FFR_i position, P_i is finally decided as the most suitable one with minimum ξ among the available P_{FFR} . The entire computation process for deciding the ith optimal FFR position is shown in **Algorithm 1** and it is performed repeatedly until the MC reaches the target location. The fluidic flow speed data inside the vessel channel at different inlet velocity data, $V_{\rm f}$, and the magnetic force distribution, \mathcal{F} are obtained from FE simulation software (COMSOL Inc., MA, USA) with simulation constraints as listed in Table 1 (as shown in Figure 4 and S1, Supporting Information). Additionally, Algorithm 1 was implemented in MATLAB R2018a.

2.1.3. FFR Generation

To produce the three-dimensional FFR, the EnEMAs consisting of nine electromagnetic coils is applied, and the specifications of

Algorithm 1. Targeting Parameters Optimization.

```
Inputs: V<sub>f,data</sub>, F, x<sub>d</sub>
Output: Pi
for i = 1:nor
        VfRF ← FldVeloAt (BFi, Vfdata)
        A_{\text{FFR}} \leftarrow - Sign \text{ (path(2, find(path(1,:) > BF_i(1)))}
        \nu_{\text{nf,BF}} \leftarrow Rot_z(A_{\text{FFR}} * \pi/2) \cdot \nu_{\text{f,BF}}
        a_i \leftarrow BF_i - R_i \cdot \nu_{f,BF}
        b_i \leftarrow BF_i + R_i \cdot \nu_{f,BF}
        for FFR_v = -2R_i : 2R_i
                 for FFR_v = R_i: \gamma_{max}
                      P_{\text{FFR}} \leftarrow a_i + FFR_x \cdot v_{\text{fBF}} + FFR_y \cdot v_{\text{nfBF}}
                      if P_{FFR,x} \in [-40,40], P_{FFR,y} \in [-20,20]
                          P_{\text{FFR}} = P_{\text{FFR}}
                      else return
                      end if
                     \mathbf{x}(0) \leftarrow a_i + A_{\text{FFR}} \cdot R_i \cdot [0,1];
                      while \mathbf{x}(t) \in [a_i : b_i] do
                          F_m \leftarrow MagForceAt (x(t-1), P_{FFR}, \mathcal{F})
                          v_f \leftarrow FldVeloAt (MCPrvPos, V_{f,data})
                          \mathbf{x}(t) = \frac{L}{K}t + \frac{\nu_0 K - L}{\nu^2} \{1 - e^{-Kt}\}\
                                                                             ►See (1)-(10)
                          if IsCollision2ChannelWall(x(t), ChnWl)
                          \mathbf{x}_{col} \leftarrow polyxpoly(\mathbf{x}(t), \mathbf{x}(t-1) \ ChnWl)
                          \textbf{if } \textit{EucliDist}(\textbf{x}_{col},\textbf{x}(t-1)) < \textbf{x}(t)
                              \mathbf{x}(t) = \mathbf{x}_{col};
                          end if
                      end if
                      \xi \leftarrow \mathbf{x}(t) - \mathbf{x_d}(t)
                 end while
             end for
        \mathsf{FiltData}_{\mathsf{Cri1}} \leftarrow^{t_{ei}}_{t_{si}} P_{\mathit{FFP}}(find(A_{\mathit{FFR}}(^{t_{ei}}_{t_{si}}\mathbf{x} - b_i)) > 0)
        FiltData_{Cri2} \leftarrow FiltData_{Cri1}(find(abs(t_i, \mathbf{x} - b_i)) < d_{lim})
        P_i \leftarrow min(FiltDataCri2(\xi))
                                                                              ▶Three criteria
end for
```

Table 1. Simulation constraints used in optimal FFR scanning.

Symbol	Quantity	Description
μ_{fluid}	0.001 Pa.s	Fluid dynamic viscosity
d_{p}	350 µm	Diameter of the MC
$ ho_{m}$	$1000 kg m^{-3}$	Density of the MC
$M_{\rm sat}$	$37.5\mathrm{emu}\mathrm{g}^{-1}$	Saturated magnetization value of MC
μ_0	$4\pi 10^{-7} H m^{-1}$	Magnetic permeability of vacuum
$ u_{\rm inlet}$	$2-20 \text{mm s}^{-1}$	Flow velocity set at inlet
Α	35 1 T ⁻¹	Langevin slop parameter of MC

the system can be found in our previous works. [39,40] The system is capable of 5-DOF motion control of magnetic objects with maximum magnetic field, 174 mT, and gradient field, 5 T m⁻¹. Let us first consider governing equations to create the magnetic and gradient field at a point, p(x, y, z), inside the workspace of the system as

2640457, 2024, 5, Downloaded from https://onlinelibrary.wiley.com/doi/1.01002/aisy.20230700 by Daegu Gyeongbuk Institute Of, Wiley Online Library on [25/10/2024]. See the Terms and Conditions (https://onlinelibrary.wiley.com/terms-and-conditions) on Wiley Online Library for rules of use; OA articles are governed by the applicable Creative Commons License,

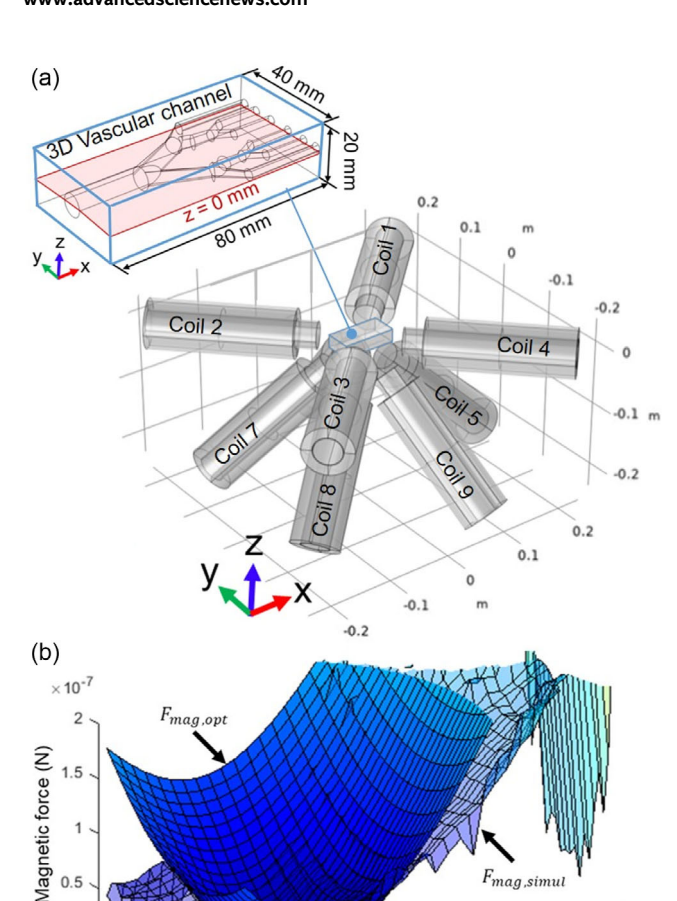


Figure 4. a) FE simulation setup of the EnEMAs with the 3D vascular channel placed inside of its workspace. b) The 3D surface map of the magnetic force used in the optimization algorithm, $\mathbf{F}_{\text{mag,opt}}$ and the magnetic force generated by the FE simulation, $\mathbf{F}_{\text{mag,simul}}$ in case of the path 1 at the inlet flow speed of 2 mm s⁻¹ as depicted in Figure S2, Supporting Information.

-20

$$\begin{cases}
\tilde{B}_{1x}i_1 + \tilde{B}_{2x}i_2 + \dots + \tilde{B}_{nx}i_n = \mathbf{B}_x(p) \\
\tilde{B}_{1y}i_1 + \tilde{B}_{2y}i_2 + \dots + \tilde{B}_{ny}i_n = \mathbf{B}_y(p) \\
\tilde{B}_{1z}i_1 + \tilde{B}_{2z}i_2 + \dots + \tilde{B}_{nz}i_n = \mathbf{B}_z(p) \\
\begin{pmatrix}
\frac{\partial \tilde{B}_{1x} + \partial \tilde{B}_{1y} + \partial \tilde{B}_{1z}}{\partial x}
\end{pmatrix} i_1 + \dots + \begin{pmatrix}
\frac{\partial \tilde{B}_{nx} + \partial \tilde{B}_{ny} + \partial \tilde{B}_{nz}}{\partial x}
\end{pmatrix} i_n = \mathbf{G}_x(p) \\
\begin{pmatrix}
\frac{\partial \tilde{B}_{1x} + \partial \tilde{B}_{1y} + \partial \tilde{B}_{1z}}{\partial y}
\end{pmatrix} i_1 + \dots + \begin{pmatrix}
\frac{\partial \tilde{B}_{nx} + \partial \tilde{B}_{ny} + \partial \tilde{B}_{nz}}{\partial y}
\end{pmatrix} i_n = \mathbf{G}_y(p) \\
\begin{pmatrix}
\frac{\partial \tilde{B}_{1x} + \partial \tilde{B}_{1y} + \partial \tilde{B}_{1z}}{\partial z}
\end{pmatrix} i_1 + \dots + \begin{pmatrix}
\frac{\partial \tilde{B}_{nx} + \partial \tilde{B}_{ny} + \partial \tilde{B}_{nz}}{\partial z}
\end{pmatrix} i_n = \mathbf{G}_z(p)
\end{cases}$$

where, \tilde{B}_{jx} , \tilde{B}_{jy} , \tilde{B}_{jz} and, $\partial \tilde{B}j/\partial x$, $\partial \tilde{B}j/\partial \gamma$ $\partial \tilde{B}j/\partial z$ are the x, γ , and z terms of unit-current magnetic field and gradient field values at point p generated by coil j^{th} , respectively. i_j is the current applied to the coil j^{th} , n is the number of electromagnetic coils used in the EnEMAs (n=9). $\mathbf{B}_x(p)$, $\mathbf{B}_y(p)$, $\mathbf{B}_z(p)$, and $\mathbf{G}_x(p)$, $\mathbf{G}_y(p)$, $\mathbf{G}_z(p)$ are the x, y, and z terms of the resultant magnetic field and gradient

field at point p induced by n number of coils, respectively. To create FFR at p, three field terms $\mathbf{B}_x(p)$, $\mathbf{B}_y(p)$, and $\mathbf{B}_z(p)$ have to be set as zeros. Thus, Equation (14) can be expressed again in FFR control form as follows

$$\begin{bmatrix} \tilde{\mathbf{B}} \mathbf{x}(p) \\ \tilde{\mathbf{B}} \mathbf{y}(p) \\ \tilde{\mathbf{B}} \mathbf{z}(p) \\ \nabla \tilde{\mathbf{B}} \mathbf{y}(p) \\ \nabla \tilde{\mathbf{B}} \mathbf{y}(p) \\ \nabla \tilde{\mathbf{B}} \mathbf{y}(p) \end{bmatrix} \begin{bmatrix} i1 \\ i2 \\ \vdots \\ in \end{bmatrix} = \begin{bmatrix} \mathbf{0}_{3 \times 1} \\ \mathbf{G}_{3 \times 1} \end{bmatrix} \Leftrightarrow \mathbf{X}(p)\mathbf{I} = \mathbf{A}$$

$$(15)$$

where, $\tilde{\mathbf{B}}_{x}(p)$ $\tilde{\mathbf{B}}_{y}(p)$, $\tilde{\mathbf{B}}_{z}(p)$ and, $\nabla \tilde{\mathbf{B}}_{x}(p)$, $\nabla \tilde{\mathbf{B}}_{y}(p)$, $\nabla \tilde{\mathbf{B}}_{z}(p)$ are the $1 \times n$ unit-current magnetic field and gradient field matrices at point p along x, y, and z axes, generated by each coil at 1 A in EnEMAs. The derivation of these dimensionless matrices, characterized as the magnetic and gradient fields, can be acquired by the FE model-based estimation technique. However, a precise estimation of an arbitrary point inside the workspace in real-time is a complex task since the database consists of the unitcurrent field and gradient field at every point in the workspace is required. An expansive database featuring an intricately woven point cloud contributes to enhanced accuracy in matrix estimation. However, this comes at the cost of extensive computational time required for data interpolation. Conversely, estimation rooted in a smaller database with sparse point coverage offers expedited calculations, albeit at the expense of estimation precision. In response to this challenge, a method is proposed to cope with this problem, which facilitates rapid yet highly accurate estimation of requisite data for subsequent steps in the current mapping process, based on the foundation of a comprehensive database. This innovative approach seeks to strike a harmonious balance between computational efficiency and estimation accuracv. The EnEMAs is first modeled with the COMSOL Multiphysics (COMSOL Inc., MA, USA) with unit current applied (1 A). Then, a database of k points, DB (15 \times k), in the workspace of the system is exported. At each point, a $12 \times n$ matrix consists of three magnetic field terms $(\tilde{\mathbf{B}}_{x}, \; \tilde{\mathbf{B}}_{y}) \; \tilde{\mathbf{B}}_{z}$ and nine gradient field terms $(\partial \tilde{\mathbf{B}}_x/\partial x, \partial \tilde{\mathbf{B}}_x/\partial y, \partial \tilde{\mathbf{B}}_x/\partial z, \partial \tilde{\mathbf{B}}_y/\partial x,$ $\partial \tilde{\mathbf{B}}_{v}/\partial y$, $\partial \tilde{\mathbf{B}}_{v}/\partial z$, $\partial \tilde{\mathbf{B}}_{z}/\partial x$, $\partial \tilde{\mathbf{B}}_{z}/\partial y$) $\partial \tilde{\mathbf{B}}_{z}/\partial z$ generated by n coils, so-called query point's unit-matrix X(p). A searching-window method (Searching Window) is applied on the database to narrow the size of the dataset, hence reducing the calculation time while maintaining the estimation accuracy. It filters out all of the dataset outside its window defined by its center located at query point, p, its width, w, and height, h, where w and h are experimentally selected as 5 mm. All of the point clouds remaining inside this window, D, are fed to the trilinear scattered interpolation method (ScatteredIntepolant) for the estimation of X(p). The currents needed for FFR generation at query point p can be simply calculated by pseudo-inverse of Equation (15). However, the FFR prefers to have an isotropic shape that conventional pseudo-inverse method hardly can produce. To improve it, we devised an algorithm for FFR optimization to minimize the gradient differences between three basic directions, i.e., $G_x(p)$, $\mathbf{G}_{\nu}(p)$, $\mathbf{G}_{z}(p)$, with the initial condition as in Equation 15 and boundary conditions (I_{max} : 20 A, I_{min} : -20 A). The details of the FFR optimization are shown in Algorithm 2.

20

x (mm)

20

y (mm) 0

of use; OA articles are governed by the applicable Creative Commons License

ADVANCED INTELLIGENT SYSTEMS

www.advancedsciencenews.com www.advintellsyst.com

Algorithm 2. Isotropic FFR Optimization.

The algorithm for FFR optimization was implemented in MATLAB R2018a by utilizing the built-in nonlinear programming solver, called *fmincon* function in the Optimization

Toolbox. As a result, the algorithm can find a solution of FFR at query point from database within 25 ms. **Figure 5** demonstrates the simulation results of the proposed method in comparison to the conventional pseudo-inverse method in terms of isoperimetric factor, response time, and position error. The size and shape of FFR generated by the optimization method is relatively smaller and more isotropic with faster calculation and higher accuracy than that of conventional method, as shown in Figure 5.

3. Optimization Results and FE Simulation Validation

The FE simulations were conducted to evaluate the feasibility of the proposed FFR scanning strategy to drive MC through multiple bifurcation channels. To ensure the same hydrodynamic

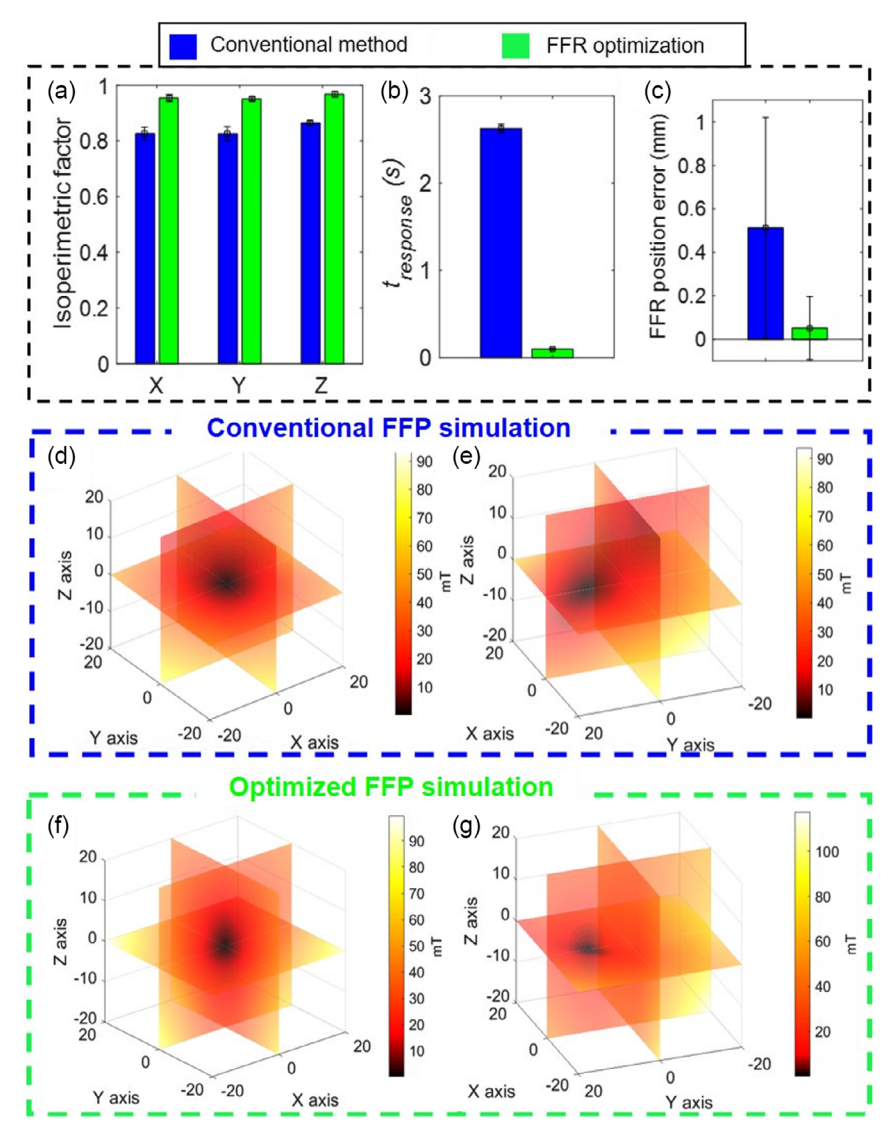


Figure 5. Comparison results of FFR generation between the conventional pseudo-inverse method and the optimization method. a) Difference between two methods in term of FFR isotropic factor. b) Response time of two methods in various cases. c) Estimated position errors of FFR center. The blue bars represent the conventional pseudo-inverse method and the green bars denote the optimization method. Three-dimensional images illustrate the simulated FFR generated by the conventional pseudo-inverse method at d) p (0,0,0) and e) p (0,10,0) and by the proposed optimization method at f) p (0,10,0) and g) p (0,10,0).

www.advancedsciencenews.com

www.advintellsyst.com

conditions, all the simulations were performed under the assumptions that the velocity profile of the fluid flow at the inlet is uniform, i.e., it starts to develop from the inlet. In addition, the surface of the channel wall and the fluid flow were assumed to be non-slip boundary condition and an incompressible laminar flow with a low Reynolds number, respectively. The pressure at all outlets was set as 1 atm, which means that all the outlets are open, and the magnetic force map used in the theoretical calculation was assumed to be radially symmetric with respect to the origin of the FFR. Therefore, the magnetic force map can be considered as a paraboloid-like surface of revolution having an axis normal to the XY plane and crossing the XY plane at the origin of the FFR (as shown in Figure 4b and S2, Supporting Information). For solid validation, the FFR magnetic force map exerted on the MC can be calculated based on the FFR magnetic field map and the magnetic properties of the MC for each case. In addition, the FFR targeting parameters in the FE simulation validation are slightly modified based on the theoretical calculation to achieve the successful targeting performance.

Figure 6 shows simulation results of applying solutions found by Algorithm 2 for targeting to six outlets in Figure 3 with inlet speed, v_{inlet} , set as 20 mm s⁻¹, including solutions for optimal FFR position and its associated timing at each FCR. Figure 6d-f,j-l illustrates the optimal FFRs positioned around the corresponding FCR, denoted as red circle, and depict the theoretically induced magnetic force (red arrows) exerted on a magnetic particle. The MC waypoints (green dashed line) during the targeting process at each FCR demonstrate the success of steering the MC toward the desired path. Details of the theoretical solutions for the targeting tasks with inlet flow speed of $20 \,\mathrm{mm \, s^{-1}}$, including the predicted shooting time, t_i , FFR shooting period, Δt_i in each FCR, are shown in Table S1, Supporting Information. Figure 6a-c illustrates the stepwise FE simulation results of the FFR targeting operation at each bifurcation under 20 mm s⁻¹ inlet velocity reaching the OL2. It can be seen that the MC particle started from the middle of the inlet and was tilted in its moving orientation along the desired path by applying the magnetic force at the shooting time. In the FE simulation, the magnetic force shooting time was modified to start when the MC reached not exactly but around the bifurcation position. The magnetic maps generated by the FFR at the shooting time of each bifurcation (t_1 , t_2 , and t_3) are shown in the background of the channel scheme. The MC, marked by the red dot, is compelled to attain the designated outlet, OL2. This trajectory, delineated by the red line, is guided by the modified targeting parameters derived from the previously mentioned theoretical calculations. The origin of the FFR and the magnetic force vector are represented by the red-cross line and the black arrows, respectively. Figure 6g-i,m-o shows the FE simulation results of the MC motion of all six paths under inlet flow velocity of 20 mm s⁻¹. As shown in Figure 6, the MC in all cases was achieved to be targeted to the intended destination by the modified FFR targeting parameters. The total targeting time through multiple bifurcations at flow speed of $20 \, \text{mm s}^{-1}$ is about $3 \, \text{s}$. Thus, it can be verified that the FE simulation results are well-matched to the theoretical calculation results with some minor errors in the targeting parameters. Furthermore, additional simulations were implemented using different inlet flow speeds to investigate the adaptiveness of the proposed strategy in various environmental conditions. The optimization results for different flow speeds of 10, 5, and 2 mm s⁻¹ can be found in Figure S3–S5 and Table S2–S4, Supporting Information. The targeting performance at the rest of the inlet velocities based on the magnetic field map and the corresponding magnetic force map are described in Figure S6–S29, Supporting Information.

Figure 6p-s illustrates the theoretical calculation of FFR targeting parameters and evaluation results utilizing FE model targeted six outlets under varying inlet flow speeds. Here, the comparison between the theoretical calculation and model validation primarily focuses on the FFR shooting time and total targeting time. Figure 6p shows the percentage differences in total targeting time between the theoretical calculation and FE validation results $(\%[\sum t_{Cal} - \sum t_{FE}] = 100 \times |\sum t_{Cal} - \sum t_{FE}|/$ $\{\sum t_{\rm Cal} + \sum t_{\rm FE}/2\}$). Figure 6q–s depicts the percentage differences in predicted FCR shooting time at the first, second, and third bifurcation (%[$t_{i,Cal} - t_{i,FE}$], i:1,2,3). Overall, the simulation results align well with the theoretical calculation exhibiting relatively small differences with average of less than 10%. In particular, at the injection flow speed of 10 mm s⁻¹, the prediction accuracy is highest with the smallest average percentage differences at six outlets among the other speeds as 2.5%, 1.9%, 3.7%, and 2.1% for total targeting time, Σt , predicted shooting time at first bifurcation, t_1 , second bifurcation, t_2 and third bifurcation, t_3 , respectively. The prediction results at 5 and 2 mm s⁻¹ account for the second and third highest accuracy with average percentage differences for Σt , t_1 , t_2 , and t_3 between theoretical calculation and FE simulation at six outlets as 8.7% versus 3.1%, 3.9% versus 10.8%, 3.9% versus 2.8%, and 2.4% versus 2.8%, respectively. In a similar manner, the prediction results at 20 mm s^{-1} exhibit the lowest accuracy with average percentage differences as 3.4%, 14.3%, 7.4%, and 3.3% for Σt , t_1 , t_2 , and t_3 , respectively. Even the worst case, at 20 mm s⁻¹, the average differences among six outlets of these four factors are 0.1, 0.12, 0.125, and 0.07 s, respectively. In detail, targeting parameter comparison between optimization results and FE evaluation under flow speed of 10, 5, and 2 mm s⁻¹ can be found in Table S2-S4, Supporting Information. In addition, Figure S30, Supporting Information, shows the theoretical prediction of the FFR shooting periods in comparison with validation result using FE model. It can be seen that the discrepancies in FFR shooting time at a certain bifurcation are always smaller than its shooting period. These findings indicate that the theoretically calculated FFR can still be affected in the FCR to steer the MC to desired direction, despite the minor difference between the prediction value and the FE model.

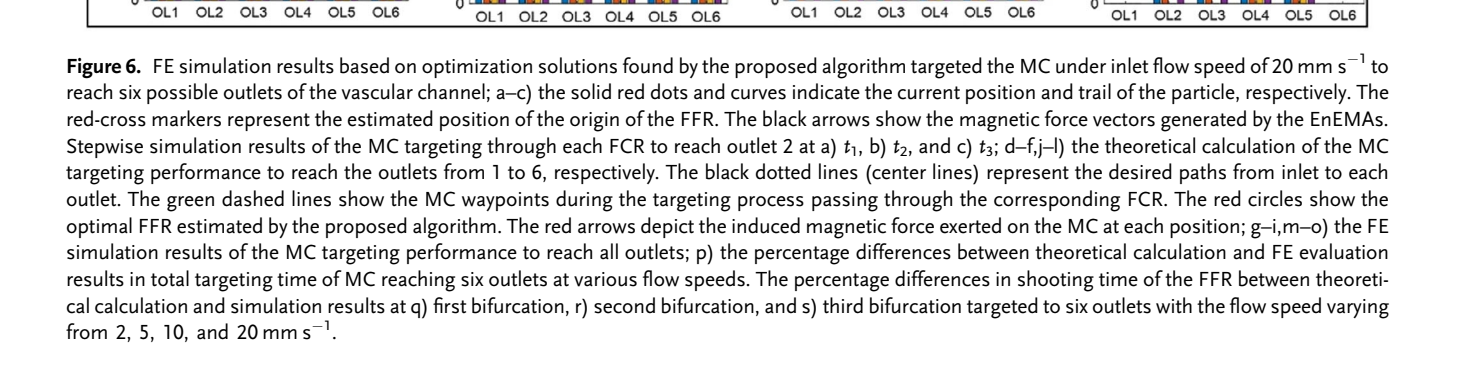
4. In Vitro Targeting Results

In vitro targeting experiment was performed based on the solution found by the optimization algorithm and confirmed by the FE simulation. Figure 7 shows the experimental setup for the targeting test in a 3D-printed vascular channel. The vascular channel of similar size to the one considered in the optimization algorithm and the FE model was printed from a transparent material (Fullcure720, Stratasys, US). A programmable syringe pump (Fusion 4000, Chemyx Inc., USA) with a 30 mL syringe (ID: 21.69 mm, Shichang medical Co., Ltd) containing DI water

26404567, 2024, 5, Downloaded from https://onlinelibrary.wiley.com/doi/10.1002/aisy.202300700 by Daegu Gyeongbuk Institute Of, Wiley Online Library on [25/10/2024]. See the Terms

nditions) on Wiley Online Library for rules of use; OA articles are governed by the applicable Creative Commons License

4DVANCED



(r) 12

2,FE

_€ 10

(q) 20

8

(S) 12

- t3.FE

€ ¹⁰

ξ, _ /8) ξ

10mm/s

(p)12

€ 10

8

2

ZIE.

% [\(\St_{\text{Ca}}\) - \(\St_{\text{Ca}}\)

ADVANCED Intelligent Systems

www.advancedsciencenews.com www.advintellsyst.com

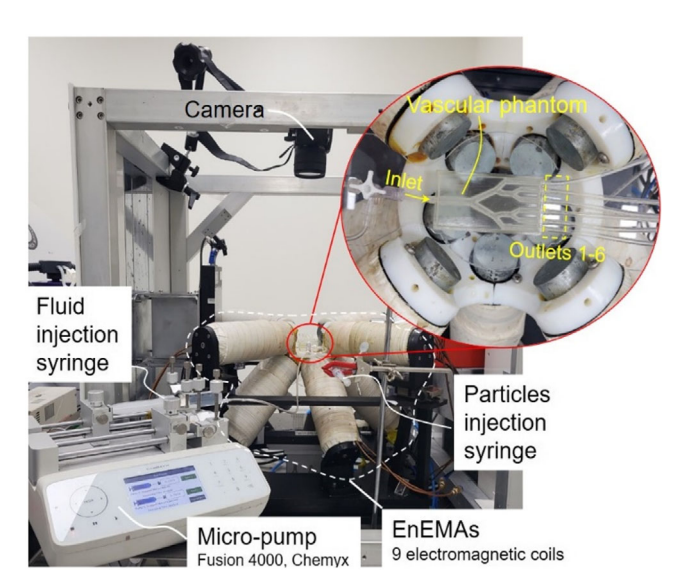


Figure 7. Experimental setup for realization of the targeting scheme using the 3D-printed vascular phantom placed inside EnEMAs working space (red circle). White dashed bounded region shows the EnEMAs which is used to create FFR at a desired position.

was used to control the flow rate inside the channel. The MC was injected by another 3 mL syringe (ID: 8.66 mm, Koreavaccine Co., Ltd) containing MCs, which were connected to the inlet of the channel. The flow rate of the pump with 30 mL syringe was set as 60.3 mL min⁻¹ to create the flow speed of 20 mm s⁻¹ at the channel inlet. A flow speed of 20 mm s⁻¹ was chosen for the experiment due to its proximity to the typical range of actual venous blood flow, which varies from 1.5 to 7.1 cm s⁻¹. [42] The vascular channel was placed inside the work space of the EnEMAs and, in advance, a coordinate matching process was worked to fit the channel coordinate to the EMAs coordinate. A digital single-lens reflex (DSLR) camera (Canon EOS 600D) with a macrolens (Canon EF 100 mm, f/2.8) was set on top of the EnEMAs to record the MC motion inside the channel. The MCs were fabricated using the water-in-oil-in-water

emulsion of poly lactic-co-glycolic acid (PLGA) and gelatin and flow control method. The MC has a porous structure to increase the amount of magnetic nanoparticles attached to its surface. The average diameter, saturated magnetization, and mass concentration of the MC are listed in Table 1.

In the targeting experiment, first, after a user designates the desired outlet and injection speed, the proposed targeting scheme starts when the MC is manually injected and it is recognizable at the inlet of the channel. The FFR is then generated at computed optimal position and shooting time. Figure 8 describes the successful trials of the targeting task utilizing the proposed FFR scanning strategy to six different outlets of the vascular channel under flow speed of 20 mm s⁻¹. The time-lapse image of the MC and its waypoints (denoted as white dashed lines) clearly demonstrates that the proposed targeting method can successfully steer a single MC to the desired destinations in the predefined multibranch channels. Consequently, the recorded targeting times were 3.06, 2.87, 2.87, 2.93, 2.87, and 3.12 s from OL1 to OL6, respectively, and these resulted in a yield of nearly 100% on effective targeting through first, second, and third bifurcation.

5. Discussion

The proposed targeting strategy was successfully implemented and validated with a single magnetic particle in various targeted branches under different flow speeds. The FFR scanning-based targeting methodology in this work is more efficiency than that of directional magnetic force control method in term of power consumption with 43% lower in power requirement to create sufficient gradient field at the same point (as shown in Figure S32 and Table S5, Supporting Information). Furthermore, it can align seamlessly with one of the most promising particle tracking techniques, MPI offering exceptional performance characteristics. This alignment presents an opportunity to integrate the proposed method with MPI, thereby creating a novel targeting scenario featuring real-time feedback on the position information of magnetic nanoparticles.

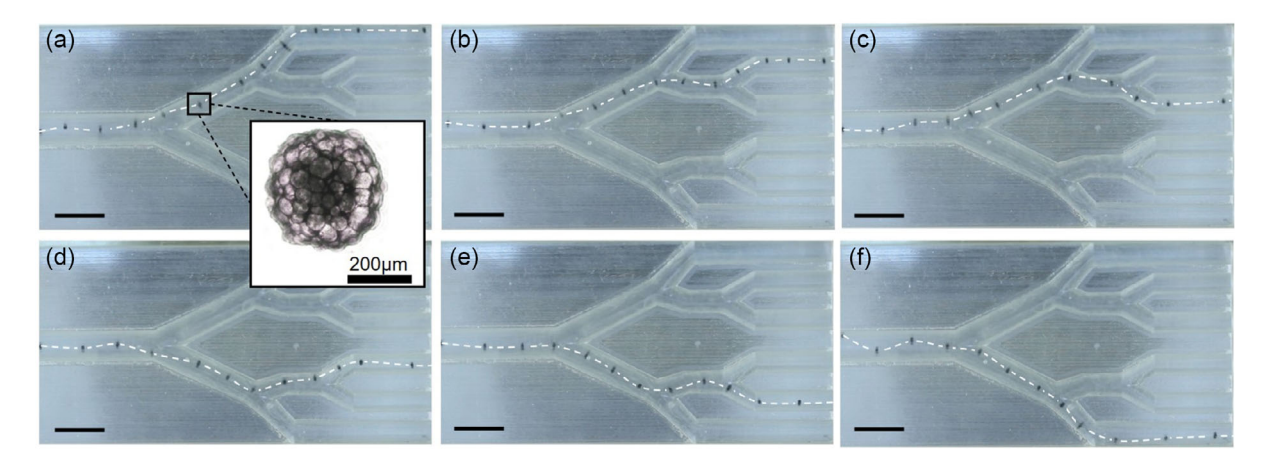


Figure 8. Time-lapse images during the targeting tasks in a 3D-printed vascular channel following a given path to six different outlets; a) outlet 1, b) outlet 2, c) outlet 3, d) outlet 4, e) outlet 5, and f) outlet 6, respectively. In (a), the dark rectangular box shows a closed-up of the MC used in this work. The white dashed curves represent the waypoints of the MC in each case. The scale bar indicates 10 mm.



www.advancedsciencenews.com

geting scheme. However, the FFR timing algorithm is currently limited to a single particle only, making it unsuitable for targeting multiple MCs. This is due to random distribution of the MCs at the inlet and tendency to move independently rather than aggregate and move together. Consequently, the arrival time of each MC to the FCR may vary. To address this challenging issue for multiple MCs targeting, an alternative timing algorithm is required to predict the appropriate FFR shooting time and shooting period to target a cluster of MCs through multiple bifurcation in a predefined vascular channel. In tandem with this computational solution, an alternative avenue emerges in the form of MC trapping and aggregation. This technique involves the strategic deployment of an On/Off maneuverable magnetic coil situated at the MC injection outlet. The dipole–dipole inter-

action among the MCs, once trapped, facilitates their aggregation

into a cluster. As a result, they can be effectively targeted using

the proposed method. These solutions aim to overcome the lim-

itations of the current FFR timing algorithm and accommodate

the complexities associated with targeting multiple MCs. By

developing a suitable timing algorithm and implementing the

MC trapping and aggregation technique, the proposed strategy

can be extended to enable efficient targeting of clusters of

MCs in complex vascular networks.

The FFR position can be optimized for multiple particles tar-

The FE simulation was conducted under some assumptions to simplify the problems. First, the FE simulation was conducted in a 2-dimensional study corresponding to the targeting strategy proposed in this work. However, to mirror real-world applications, which encompass the intricacies of a three-dimensional vascular network, the full 3-dimensional study should be undertaken in forthcoming investigations. Second, the interaction between the particle and the surrounding fluid flow was not considered in this study, such as vortices forming around the particles, particularly in proximity to the channel wall within the bifurcation region. This might cause the difference between the FE simulations. This could be resolved by adopting the hydrodynamic mobility tensor coupling. [43] Lastly, the adhesive interaction between the channel wall and the MC particle was excluded from the FE simulation. This omission might contribute to the divergence between the simulation results and realworld observations. Mitigating this discrepancy could involve the integration of adhesion models governing particle-wall interactions.[44]

The disparities noted between the theoretical predictions and FE model simulation results can be attributed to certain assumption made at FCR. In the FCR, it is presumed that the MCs consistently remain in the worst-case scenario, leading to an extended FFR shooting time compared to what was anticipated. While this assumption is essential for a multiple particle targeting scheme, it may contribute to the observed differences. A notable challenge encountered during in vitro navigation of the MCs, leading to test failures, pertains to the surface adhesion of the MCs to the channel wall. This aspect was intentionally omitted from consideration due to the intricate nature of surface properties linked to fluid viscosity, rendering accurate mimicry in real-world experiments extremely challenging. Moreover, there is a dearth of previous references concerning the friction model and interaction between particles and the vessel channel wall. Empirical observations suggest that surface friction www.advintellsyst.com

between the MC and the channel is more pronounced at low injection speeds compared to higher injection speeds, with rare occurrences observed at the flow speed of 20 mm s⁻¹. However, when such instances do arise, the targeting scheme employing optimized FFR parameters struggles to adapt to this situation, resulting in a shift in particle motion. Consequently, the MC may become immobilized at a specific point within the channel. Additionally, the head losses incurred at sudden enlargement, particularly at the inlet connector, pose a challenge during the in-vitro experiment. This phenomenon generates recirculation zones near the enlarge area of the inlet (refer Figure S31, Supporting Information, for more details). The change in flow dynamic associated with these recirculation zones can significantly affect to the trajectories of the MC.^[45] Certain particles might even experience a complete lack of motion within these regions. To mitigate the influence of sudden expansion head losses, a gradual expansion of the channel is implemented from the connection point. This strategy aims to minimize disruptions in flow dynamics, diminish pressure gradients, and optimize particle transport efficiency through channel geometry. Mismatch in FFR position control can also be a significant factor contributing to errors in the targeting task. Two potential issues may give rise to this position error. First, there may be a mismatch between the gradient and magnetic field input and the applied current output due to the employed mapping algorithm. Second, system errors may arise from the primary misalignment of the fabricated coil in comparison to the desired system. In this study, the utilized mapping algorithm demonstrates a relatively small FFR position error compared to the conventional algorithm, with position errors of 0.1 and 0.5 mm, respectively. The primary system error of this EnEMAs was previously analyzed in our earlier works, [39,40] revealing a propulsion error of 1.05° and a mean FFR-controlled position error of 1.3 mm. The details of the simulated FFR position and the desired FFR position considered in this study can be found in Figure S6-S29 and Table S1-S4, Supporting Information. Generally, the FFR position errors in these cases are not significant enough to adversely affect targeting accuracy.

Despite the minor disparities in predicted FFR timing values, FE model evaluation outcomes, and in vitro navigation test, the proposed targeting scheme consistently performed well across most tests explored in this study. As long as the variations in FFR shooting time at specific bifurcation points do not exceed their respective shooting periods, the targeting scheme demonstrates its efficacy.

6. Conclusion

The FFR scanning strategy in this study was demonstrated to effectively guide the magnetic particle from injection point through intricate vascular networks, encompassing multiple bifurcations, irrespective of particle's visual position feedback. This approach holds significant promise for augmenting treatment efficiency and minimizing adverse effects. The method's applicability extends to a broad spectrum of existing electromagnetic navigation systems, rendering it poised for scalability and potential application within in vivo scenarios. The primary challenge inherent in this proposed method pertains to the initial

26404567, 2024. S. Downloaded from https://onlinelibrary.wiley.com/doi/10.1002/aisy.202300700 by Daegu Gyeongbuk Institute Of, Wiley Online Library on [25/10/2024]. See the Terms and Conditions (https://onlinelibrary.wiley.com/terms

and-conditions) on Wiley Online Library for rules of use; OA articles are governed by the applicable Creative Commons License

www advancedsciencenews com

www.advintellsyst.com

system setup, necessitating considerable effort to gather environmental parameters. Nevertheless, this challenge is not insurmountable from a technical standpoint and can be addressed using available techniques. Subsequent directions for this research will concentrate on multiple MC targeting in a complex 3D vascular network and translating this method into an animal model setting.

Supporting Information

Supporting Information is available from the Wiley Online Library or from the author.

Acknowledgements

K.T.N. and H.K. contributed equally to this work. This work was supported by the Korea Medical Device Development Fund grant funded by the Korea government (the Ministry of Science and ICT, the Ministry of Trade, Industry and Energy, the Ministry of Health & Welfare, the Ministry of Food and Drug Safety) (project number: 1415181807, RS-2021-KD000001), and by the Technology Innovation Program (or Industrial Strategic Technology Development Program) (20017903, Development of medical combination device for active precise delivery of embolic beads for transcatheter arterial chemoembolization and simulator for embolization training to cure liver tumor) funded By the Ministry of Trade, Industry & Energy (MOTIE, Korea).

Conflict of Interest

The authors declare no conflict of interest.

Data Availability Statement

The data that support the findings of this study are available in the supplementary material of this article.

Keywords

magnetic field-free region, magnetic microcarriers, magnetic navigation, targeted drug delivery, vascular system

Received: October 30, 2023 Revised: February 14, 2024 Published online: April 15, 2024

- [1] S. Senapati, A. K. Mahanta, S. Kumar, P. Maiti, Signal Transduction Targeted Ther. 2018, 3, 7.
- [2] J. K. Patra, G. Das, L. F. Fraceto, E. V. R. Campos, M. D. P. Rodriguez-Torres, L. S. Acosta-Torres, L. A. Diaz-Torres, R. Grillo, M. K. Swamy, S. Sharma, S Abtemariam, J. Nanobiotechnol. 2018, 16, 71.
- [3] J. Li, L. Dekanovsky, B. Khezri, B. Wu, H. Zhou, Z. Sofer, Cyborg Bionic Syst. 2022, 2022, 9824057.
- [4] C. Huang, Z. Lai, X. Wu, T. Xu, Cyborg Bionic Syst. 2022, 2022, 0004.
- [5] B. Dutta, K. C. Barick, P. A. Hassan, Adv. Colloid Interface Sci. 2021, 296, 102509.
- [6] D. Ramadon, M. T. C. McCrudden, A. J. Courtenay, R. F. Donnelly, Drug Deliv. Transl. Res. 2022, 12, 758.
- [7] S. Liu, B. Yu, S. Wang, Y. Shen, H. Cong, Adv. Colloid Interface Sci. 2020, 281, 102165.

- [8] M. Latulippe, S. Martel, IEEE Trans. Robot. 2015, 31, 1353.
- [9] Y. L. Liu, D. Chen, P. Shang, D. C. Yin, J. Controlled Release 2019, 302, 90.
- [10] Z. Yang, L. Zhang, Adv. Intell. Syst. 2020, 2, 2000082.
- [11] S. Tognarelli, V. Castelli, G. Ciuti, C. Di Natali, E. Sinibaldi, P. Dario, A. Menciassi, J. Robot. Surg. 2012, 6, 5.
- [12] D. D. Herea, L. Labusca, E. Radu, H. Chiriac, M. Grigoras, O. D. Panzaru, N. Lupu, Mater. Sci. Eng. C 2019, 94, 666.
- [13] W. Song, X. Su, D. A. Gregory, W. Li, Z. Cai, X. Zhao, *Nanomaterials* 2018, 8, 907.
- [14] S. Kenjereš, J. L. Tjin, R. Soc. Open Sci. 2017, 4, 170873.
- [15] Z. Li, Y. P. Lai, E. Diller, Adv. Intell. Syst. 2023, 6, 2300052.
- [16] P. Zhang, W. Wang, Y. Shi, X. Yuan, Comput. Assist. Surg. 2016, 21, 143.
- [17] M. Muthana, A. J. Kennerley, R. Hughes, E. Fagnano, J. Richardson, M. Paul, C. Murdoch, F. Wright, C. Payne, M. F. Lythgoe, N. Farrow, *Nat. Commun.* 2015, 6, 8009.
- [18] A. K. Hoshiar, T. A. Le, F. U. Amin, M. O. Kim, J. Yoon, J. Magn. Magn. Mater. 2017, 427, 181.
- [19] M. D. Tehrani, M. O. Kim, J. Yoon, IEEE Trans. Magn. 2014, 50, 5100412.
- [20] M. P. Kummer, J. J. Abbott, B. E. Kratochvil, R. Borer, A. Sengul, B. J. Nelson, *IEEE Trans. Robot.* 2010, 26, 1006.
- [21] J. Nam, W. Lee, E. Jung, G. Jang, IEEE Trans. Ind. Electron. 2018, 65, 5673.
- [22] S. Jeong, H. Choi, J. Choi, C. Yu, J. O. Park, S. Park, Sens. Actuators, A 2010, 157, 118.
- [23] M. Cai, Q. Wang, Z. Qi, D. Jin, X. Wu, T. Xu, L. Zhang, IEEE Trans. Cybern. 2022, 53, 7699.
- [24] O. Erin, X. Liu, J. Ge, J. Opfermann, Y. Barnoy, L. O. Mair, J. U. Kang, W. Gensheimer, I. N. Weinberg, Y. Diaz-Mercado, A. Krieger, Adv. Intell. Syst. 2022, 4, 2200072.
- [25] J. Lu, Y. Liu, W. Huang, K. Bi, Y. Zhu, Q. Fan, Cyborg Bionic Syst. 2022, 2022, 17.
- [26] Y. X. J. Wáng, T. De Baere, J. M. Idée, S. Ballet, Chin. J. Cancer Res. 2015, 27, 96.
- [27] M. Caine, D. Carugo, X. Zhang, M. Hill, M. R. Dreher, A. L. Lewis, Adv. Healthcare Mater. 2017, 6, 1601291.
- [28] G. Go, A. Yoo, K. T. Nguyen, M. Nan, B. A. Darmawan, S. Zheng, B. Kang, C. S. Kim, D. Bang, S. Lee, K. P. Kim, Sci. Adv. 2022, 8, eabq8545.
- [29] M. Latulippe, S. Martel, in IEEE Int. Conf. on Intelligent Robots and Systems, IEEE, New York, NY 2016.
- [30] A. K. Hoshiar, T. A. Le, P. Valdastri, J. Yoon, J. Micro-Bio Robot. 2020, 16, 137.
- [31] J. Rahmer, D. Wirtz, C. Bontus, J. Borgert, B. Gleich, IEEE Trans. Med. Imaging 2017, 36, 1449.
- [32] T. Knopp, N. Gdaniec, M. Möddel, Phys. Med. Biol. 2017, 62, R124.
- [33] L. C. Wu, Y. Zhang, G. Steinberg, H. Qu, S. Huang, M. Cheng, T. Bliss, F. Du, J. Rao, G. Song, L. Pisani, Am. J. Neuroradiol. 2019, 40, 206.
- [34] O. C. Sehl, P. J. Foster, Sci. Rep. 2021, 11, 22198.
- [35] N. Panagiotopoulos, R. L. Duschka, M. Ahlborg, G. Bringout, C. Debbeler, M. Graeser, C. Kaethner, K. Lüdtke-Buzug, H. Medimagh, J. Stelzner, T. M. Buzug, *Int. J. Nanomed.* 2015, 10, 3097.
- [36] X. Zhang, T. A. Le, A. K. Hoshiar, J. Yoon, IEEE/ASME Trans. Mechatron. 2018, 23, 1573.
- [37] K. Bente, A. C. Bakenecker, A. von Gladiss, F. Bachmann, A. Cēbers, T. M. Buzug, D. Faivre, ACS Appl. Nano Mater. 2021, 4, 6752.
- [38] F. Griese, T. Knopp, C. Gruettner, F. Thieben, K. Müller, S. Loges, P. Ludewig, N. Gdaniec, J. Magn. Magn. Mater. 2020, 498, 166206.

26404567, 2024, 5, Downloaded from https://onlinelibrary.wiley.com/doi/10.1002/aisy.202300700 by Daegu Gyeongbuk Institute Of, Wiley Online Library on [25/10/2024]. See the Terms

and-conditions) on Wiley Online Library for rules of use; OA articles are governed by the applicable Creative Commons License

www.advancedsciencenews.com

www.advintellsyst.com

- [39] K. T. Nguyen, G. Go, J. Zhen, M. C. Hoang, B. Kang, E. Choi, J. O. Park, C. S. Kim, Sci. Rep. 2021, 11, 15122.
- [40] K. T. Nguyen, G. Go, M. C. Hoang, J. Ha, J. O. Park, C. S. Kim, in Int. Conf. on Control, Automation and Systems, IEEE, New York, NY 2021.
- [41] S. Garg, K. H. Kumar, D. Sahni, T. D. Yadav, A. Aggarwal, T. Gupta, Ann. Anat. 2020, 227, 151409.
- [42] M. Klarhöfer, B. Csapo, C. Balassy, J. C. Szeles, E. Moser, Magn. Reson. Med. 2001, 45, 716.
- [43] Z. M. Sherman, J. L. Pallone, R. M. Erb, J. W. Swan, Soft Matter 2019, 15, 6677.
- [44] M. Park, T. A. Le, A. Eizad, J. Yoon, IEEE Access 2020, 8, 106714.
- [45] E. Chappel, in Drug Delivery Devices and Therapeutic Systems, Academic Press, USA 2020.